

Original Research

Manganese-Enhanced MRI Reveals Multiple Cellular and Vascular Layers in Normal and Degenerated Retinas

Govind Nair, PhD,^{1,2} Mabelle T. Pardue, PhD,^{3,4} Moon Kim, BS,³ and Timothy Q. Duong, PhD^{5,6*}

Purpose: To use manganese-enhanced magnetic resonance imaging (MEMRI) at $25 \times 25 \times 800 \mu\text{m}^3$ to image different retinal and vascular layers in the rat retinas.

Materials and Methods: Manganese-chloride was injected intraocularly in normal ($n = 5$) and Royal College of Surgeons (RCS, an model of photoreceptor degeneration) ($n = 5$) rats at postnatal day 90. MEMRI at 4.7 T was performed 24 hours later. MRI was repeated following intravenous Gd-DTPA in the same animals to highlight the vasculatures. Layer assignment and thickness were compared to histology.

Results: MEMRI 24 hours after intravitreal manganese-chloride injection revealed seven bands of alternating hyper- and hypointensities, corresponding histologically to the ganglion cell layer, inner plexiform layer, inner nuclear layer, outer plexiform layer, outer nuclear layer, photoreceptor-segment layer, and choroidal vascular layer. Intravenous Gd-DTPA—which does not cross the blood–retinal barrier and the retinal pigment epithelium—further enhanced the two layers bounding the retina, corresponding to the retinal and choroidal vascular layers, but not the avascular outer nuclear layer and the photoreceptor-segment layer. MEMRI of the RCS retinas revealed the loss of the outer plexiform layer, outer nuclear layer, and photoreceptor-segment layer. Histological analysis corroborated the MRI laminar assignments and thicknesses.

Conclusion: Lamina-specific retinal structures neurodegenerative changes to structure in retinal diseases can be detected using MEMRI.

Key Words: magnetic resonance imaging; MEMRI; retinal degeneration; high resolution imaging; MRI microscopy; RCS

J. Magn. Reson. Imaging 2011;34:1422–1429.
© 2011 Wiley Periodicals, Inc.

THE NEURAL RETINA can be characterized histologically into six major distinct layers (1). From the vitreo-retinal interface, these layers are the nerve fiber layer/ganglion cell layer, inner plexiform layer, inner nuclear layer, outer plexiform layer, outer nuclear layer, and photoreceptor-segment layer. The interspersed plexiform layers are synaptic links between adjacent nuclear layers. Two flanking blood supplies nourish the retina. The retinal vasculature, located closest to the vitreous, exists predominantly within the ganglion cell layer but also projects capillaries deep into the inner plexiform layer and inner nuclear layer. In some species, including rats, deep capillaries are also sparsely present in the proximal outer plexiform layer (2). The choroidal vasculature, on the other hand, is external to the neural retina and is sandwiched between the retinal pigment epithelium (RPE) and the sclera. If considered with the six histologically defined layers, the choroidal vasculature constitutes an additional (seventh) layer. The outer nuclear layer and the photoreceptor-segment layer are avascular.

Most retinal imaging modalities, such as fundus photography and optical coherence tomography for structural imaging as well as fluorescein angiography and laser Doppler flowmetry for blood flow imaging, are based on optics. These techniques are generally limited to probing the inner retinal surface and/or large surface vessels and the signals are confounded by tissue absorption and optical scattering. Signals arising from multiple retinal layers are generally difficult to separate. Moreover, disease-induced opacity of the vitreous humor and/or lens precludes the use of optically based imaging techniques to study the retina.

¹Graduate School of Biomedical Science, University of Massachusetts Medical School and Worcester Polytechnic Institute, Worcester, Massachusetts, USA.

²Yerkes Imaging Center, Neuroscience Division, Emory University, Atlanta, Georgia, USA.

³Atlanta Veterans Affairs Medical Center, Atlanta, Georgia, USA.

⁴Department of Ophthalmology, Emory University, Atlanta, Georgia, USA.

⁵Research Imaging Institute, Departments of Ophthalmology and Physiology, University of Texas Health Science Center at San Antonio, San Antonio, Texas, USA.

⁶South Texas Veterans Health Care System, Department of Veterans Affairs, San Antonio, Texas, USA.

*Address reprint requests to: T.D., Research Imaging Institute, UTHSCSA, 8403 Floyd Curl Dr., San Antonio, TX 78229.
E-mail: duongt@uthscsa.edu

Received January 12, 2011; Accepted June 21, 2011.

DOI 10.1002/jmri.22719

View this article online at wileyonlinelibrary.com.

In contrast, magnetic resonance imaging (MRI) is widely used for noninvasive imaging of brain anatomy, physiology, and function *in vivo*. The nascent capacity of MRI to distinguish various tissue types can be further enhanced by using exogenous contrast agents. Manganese (Mn), for example, is both an MRI contrast agent and a calcium analog. Mn is trapped in the intracellular space with a half-life on the order of days (3) and thus enhances intracellular MRI signal. Mn appears to preferentially accumulate in neuronal cell bodies compared to dendritic processes by cell volume (4–6) and thus Mn-enhanced MRI (MEMRI) in the retina could in principle be used to resolve the interdispersed nuclear and plexiform layers. MEMRI of the retina following intraperitoneal administration of Mn has been used as a measure of retinal function after prolonged light and dark adaptation (7). Gd-DTPA (gadolinium-diethylene-tri-amine-pentaacetic acid) is another contrast agent widely used to selectively enhance the vascular compartment in the brain because normal blood–brain and blood–retinal barriers as well as the RPE are impermeable to Gd-DTPA (8).

In this study we explored high-contrast MEMRI to resolve rat retinal layers *in vivo* at $25 \times 25 \mu\text{m}$ in-plane resolution. Mn was injected directly into the vitreous. Seven distinct bands of alternating signal intensities were consistently detected. Three additional sets of experiments were performed to corroborate layer assignments. First, Gd-DTPA was injected intravenously to Mn-injected rats to visualize the two vascular layers bounding the retina. Second, standard histology was performed and histological layer thicknesses were obtained for cross-validation of MRI-derived layer assignments and laminar thicknesses. Finally, we investigated an established animal model of photoreceptor degeneration, the Royal College of Surgeons (RCS) rats (9). RCS rats have a genetic defect in the RPE that prevents proper phagocytosis of the photoreceptor segments, resulting in a spontaneous and complete degeneration of the photoreceptors by postnatal day 90 (P90). MEMRI detected the expected loss of the outer plexiform layer, outer nuclear layer, and photoreceptor-segment layer, consistent with histology. This study demonstrates laminar structures in the *in vivo* retina at very high spatial resolution and contrast without depth limitation.

MATERIALS AND METHODS

Animal Preparation

All experiments were performed with approval of the Institutional Animal Care and Use Committee at Emory University and in accordance with the Association for Research in Vision and Ophthalmology's statement for the Use of Animals in Ophthalmic and Visual Research. Rats were anesthetized under 2% isoflurane and isotonic MnCl_2 solution was injected into the vitreous of the left eye over 2 minutes via a 30G needle and a Hamilton syringe, which was left in place for 2 additional minutes before withdrawal. To optimize the dosage for retinal contrast enhancement, 5 μL of isotonic 20, 30, 60, or 120 mM of MnCl_2 was

injected intravitreally into the left eye of a separate group of animals ($n = 12$). Subsequent studies using the optimal dose (5 μL of 30 mM) were carried out on two additional groups of animals: 2) Sprague–Dawley rats (control, $n = 5$, P90, 275–300 g), and 2) Long–Evans RCS rats ($n = 5$, P90, ≈ 300 g) with essentially complete photoreceptor degeneration.

Although the RPE is pigmented in Long–Evans but not pigmented in Sprague–Dawley, the laminar structure of the retina does not differ on histology and thickness and thus Mn accumulation should not differ. The diameters, and thus vitreous volume, of the control and RCS retina were similar. Thus, the concentration of Mn delivered was likely similar and should not result in differences in laminar contrasts and assignments between the two strains.

After intravitreal MnCl_2 injection, animals were returned to normal housing in their cages. Approximately 24 hours after MnCl_2 injection animals were anesthetized using 2% isoflurane and a femoral vein was catheterized for remote administration of Gd-DTPA during MRI. Animals were intubated (or tracheotomized), mechanically ventilated, paralyzed with pancuronium bromide (3 mg/kg first dose, followed by 1 mg/kg/hr, *i.v.*), and placed onto a head holder consisting of ear and tooth bars. MRI was performed under 1% isoflurane anesthesia. End-tidal CO_2 (Surigivet capnometer, Waukesha, WI) and heart rate and arterial O_2 saturation (Nonin-8600, Plymouth, MN) was continuously monitored and maintained within normal physiologic ranges unless otherwise perturbed. Rectal temperature was maintained at $37 \pm 0.5^\circ\text{C}$ using a pad with warm circulating water throughout the experiments. MRI was performed before and after Gd-DTPA injection (0.4 mL/kg, 0.5 M, *i.v.*) while the Mn-injected animals were in the magnet.

MRI Experiments

MRI experiments were performed on a Bruker 4.7-T/40-cm scanner (Billerica, MA). A custom-built, small circular surface coil (I.D. ≈ 1 cm) was placed on the left eye. To minimize partial-volume effects, MRI was performed on a single image slice along the center of the retina roughly bisecting the optic nerve head. T_1 -weighted MRI used a conventional gradient-echo pulse sequence with TR = 104 msec, TE = 8.5 msec, flip angle (FA) = 30° , 0.8 mm slice thickness, 16 repetitions acquired as a time series, data matrix = 256×256 , and field of view (FOV) = 6.4×6.4 mm, yielding an in-plane resolution of $25 \times 25 \mu\text{m}$.

Image Data Analysis

Data analysis employed Stimulate software (10) and programs written in MatLab (MathWorks, Natick, MA). The time series data were corrected for motion and/or drift as needed before averaging offline. Cognizant of some partial-volume effects, the thickness of each MRI-derived band was determined as described below. Radial projections perpendicular to the vitreous boundary (8,11) were obtained with six times the

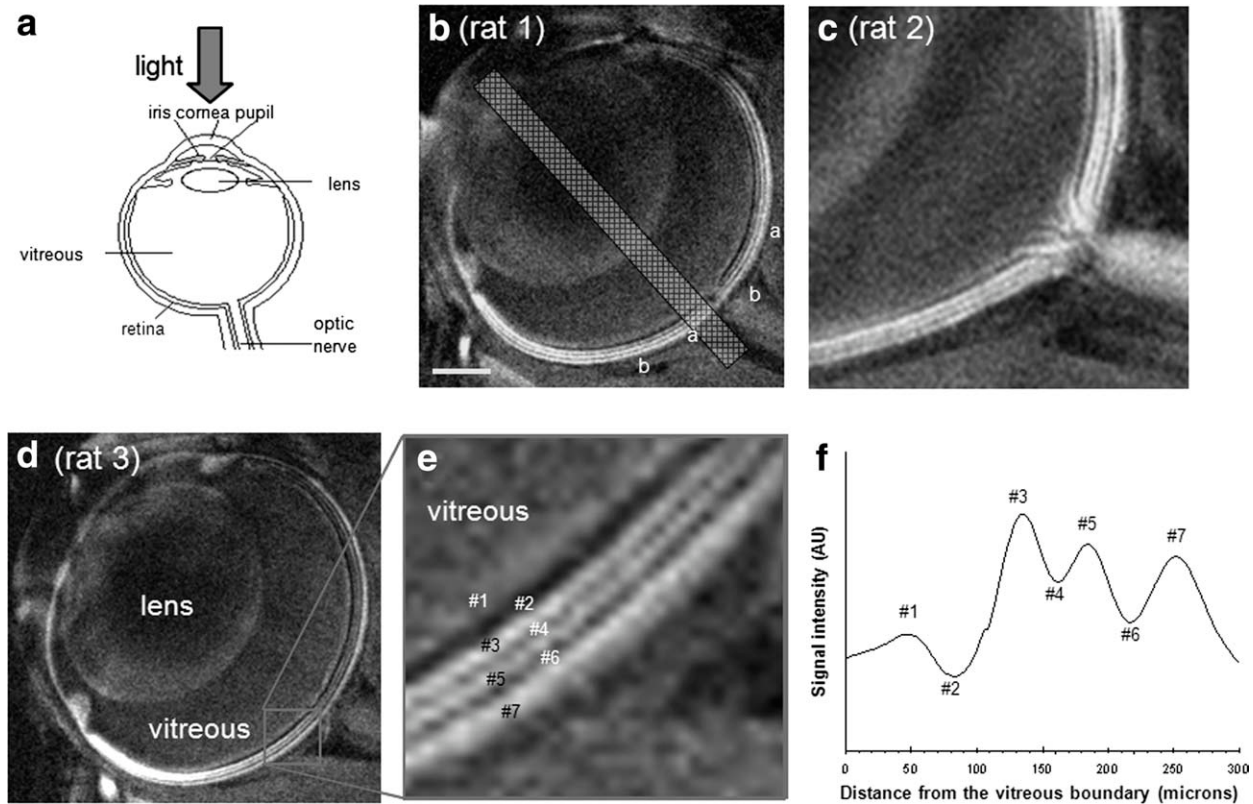


Figure 1. **a:** A schematic of the eye, showing the neural retina at the inner surface of the posterior eye cup. **b–d:** Mn-enhanced anatomical images of the retina at $25 \times 25 \mu\text{m}$ resolution from three different rats. Seven distinct bands of the retina are visible as indicated by the alternating bright and dark signal intensities. Nerves can be seen originating at the optic nerve head in one of the rats, forming the innermost diffuse hyperintense layer. **e:** Zoomed-in view of one of the rat eyes showing the layer assignment of bands #1–7. **f:** A spatial profile across the thickness of the retina from an animal intravitreally injected with MnCl_2 ≈ 24 hours earlier.

sampling density of the original image (equivalent to spatial interpolation). Signal intensities along these projections were averaged into intensity profiles. The full-width-at-half-maximum (FWHM) peak heights (assuming the baselines to be at the vitreous and sclera) were taken to be the laminar thicknesses. The thickness of the troughs was obtained using the full heights marks determined from the peaks. Although this approach had some drawbacks, such as not accounting for any rolling baseline or lack of information of the entire retina, it provided robust measures of laminar thicknesses allowing comparison between normal and diseased retinas. Thickness measurements were made from profiles plotted along a ≈ 1 mm length of the retina on either side of the optic nerve head, cognizant of the nonuniform retinal thickness from posterior pole to the pars plana.

Histology

Standard histology was obtained on approximately the same imaging slices. Following anesthetic overdose, eyes were enucleated and immersion-fixed overnight in 2% paraformaldehyde and 2.5% glutaraldehyde. Eyes were rinsed in 0.1 M phosphate buffer, dissected to isolate the posterior eyecup, and divided into two halves along the optic nerve. The eyeball was

embedded in epoxy-resin and sectioned at $0.5 \mu\text{m}$ for thickness measurement and Toluidine blue staining. Thicknesses of different layers of the neural retina and choroidal vasculature were semiautomatically derived using an image analysis program (Image Pro, Media Cybernetics, Silver Springs, MD).

RESULTS

Based on our measurement of rat eye diameter (6–7 mm), the impact of MRI slice thickness on partial-volume effect (PVE) was estimated. Assuming a 6-mm diameter sphere and 0.8-mm MRI imaging slice thickness, the maximal deviation (δ) due to curvature was $<10\%$ of total retinal thickness. Moreover, the retina is somewhat flat in the central region. Thus, for the central slice the above calculation reflects the upper limits of PVE.

The optimal MnCl_2 dose that consistently enhanced the different bands in the retina was determined to be $5 \mu\text{L}$ of 30 mM MnCl_2 when imaged 24 hours postinjection. Lower doses failed to yield consistent contrast and higher doses caused undesirable T_2^* signal decay. Using the optimal dose, high-resolution, high-contrast MEMRI of normal retinas revealed seven distinct bands of alternating hyper- and hypointensities (Fig. 1).

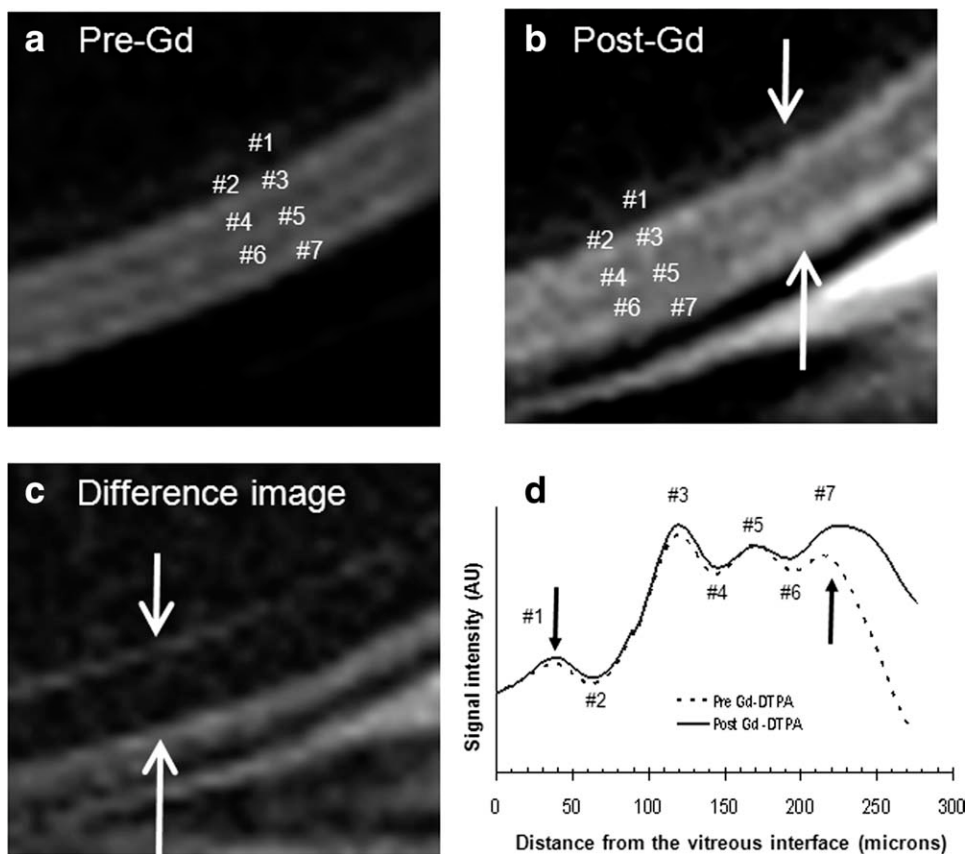


Figure 2. T_1 -weighted images at $25 \times 25 \mu\text{m}$ of an animal intravitreally injected with MnCl_2 ≈ 24 hours earlier (a) before, (b) after Gd-DTPA intravenous administration, and (c) the difference. Enhancements were observed in the bands on either side of the retina (as indicated by arrows), most evident in the difference image. d: Signal intensity profiles obtained across the thickness of the retina before and after the intravenous administration of Gd-DTPA. Modified from figure 12 in Ref. (12) with permission.

Zoomed images of the retina (Fig. 1c) clearly showed hyperintense signal from the nerves originating at the optic nerve head and forming the diffuse layer on the innermost surface of the eye in one of the control rats. The bands were numbered #1 through #7, starting at the innermost diffuse layer (Fig. 1e). Signal intensity profiles projected perpendicular to the retinal surface showed a diffuse bright band closest to the vitreous (#1) and three bright bands (#3, #5, and #7) interspersed among three dark bands (#2, #4, and #6) (Fig. 1f).

Following intravenous administration of Gd-DTPA to the Mn-injected rats, subtraction of pre- and post-Gd-DTPA images produced intensity profiles that revealed enhancement on either side of the retina (bands #1–3 and 7) (Fig. 2a–c, modified from figure 12 in Ref. (12) with permission). The outer band #7 was enhanced more by Gd-DTPA than the inner bands #1–3 (Fig. 2d). In contrast, there were no significant Gd-DTPA enhancements of the middle sections of the retina (layer #4–6) and the vitreous. The anterior segment of the eye was also enhanced due to the high permeability of the ciliary body to Gd-DTPA (data not shown), consistent with a previous report (8).

To cross-validate laminar assignments, histology was performed (Fig. 3a). Histologic section of the normal retina showed seven layers, representing the ganglion cell layer, inner plexiform layer, inner nuclear layer, outer plexiform layer, outer nuclear layer, inner + outer photoreceptor-segment layer, and the choroidal vascular layer. MRI and histologic layer assign-

ments and laminar thicknesses were tabulated and are summarized in Table 1. The seven MRI-derived bands were interpreted as corresponding to the seven layers defined by histology. The total thickness of the normal retina including the choroidal vascular layer was $275 \pm 30 \mu\text{m}$ by MRI and $251 \pm 13 \mu\text{m}$ by histology.

To further corroborate the MRI-derived laminar assignments, retinas of P90 RCS rats, in which the photoreceptors are expected to have degenerated, were investigated. In contrast to the normal retinas, MEMRI of the P90 RCS retinas revealed only four bands of alternating hyper- and hypointensities plus a debris band (Fig. 3B,C). The overall retinal thickness was markedly reduced. Comparison of the MEMRI intensity profiles revealed the disappearance of bands #4–6, diminished intensity of band #3, the appearance of a debris layer, and a thinning of the total retinal thickness in the P90 RCS retinas.

In the P90 RCS retina, the histological results showed that, in place of the outer plexiform layer (band #4), outer nuclear layer (corresponding to band #5), and photoreceptor-segment layer (band #6), only a thin debris layer was visible in the P90 RCS retina and the total retinal thickness was markedly reduced. Layer assignments and thicknesses by MRI and histology of the P90 RCS retinas were tabulated and are summarized in Table 2. The missing layers in the P90 RCS retinas were interpreted to be bands #4–6, corresponding to the outer plexiform layer, outer nuclear layer, and photoreceptor-segment layer, respectively. The total thickness including the choroidal vascular

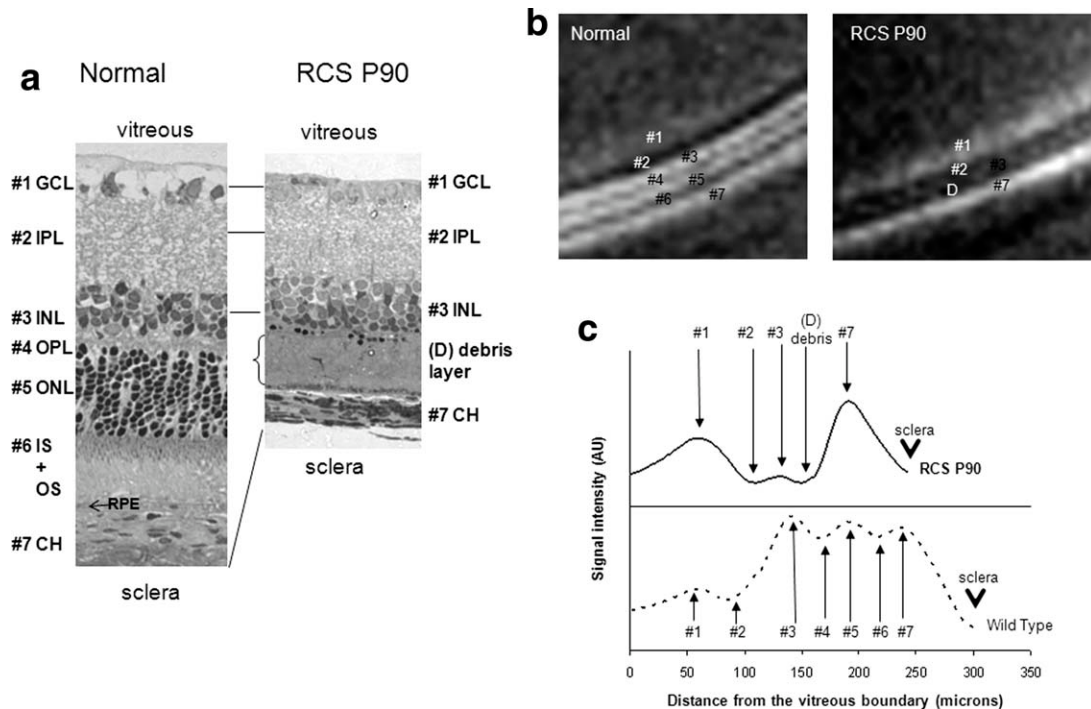


Figure 3. (a) Histology, (b) Mn-enhanced MRI, (c) signal intensity profiles from a normal and a P90 RCS retina. The layer assignments of the normal rat retina are: 1. ganglion cell layer (GCL), 2. inner plexiform layer (IPL), 3. inner nuclear layer (INL), 4. outer plexiform layer (OPL), 5. outer nuclear layer (ONL), 6. inner and outer photoreceptor segment layer (IS+OS), and 7. choroidal vascular layer (CH). RPE denotes retinal pigment epithelium. In the P90 RCS retina, bands #4–6 appeared missing and band #3 showed reduced signal intensity, whereas band #1 was slightly more enhanced, compared to the corresponding bands in the normal retina. The corresponding histological slide of the P90 RCS retina showed a debris band in place of bands #4–6 in the normal retina. Letter D indicates the debris layer. The arrowhead in c indicates the sclera.

layer of the P90 RCS retinas was $212 \pm 22 \mu\text{m}$ by MRI and 208 ± 15 by histology, significantly thinner than the normal retinas. Together, the P90 RCS rat data further corroborate the MRI layer assignments.

DISCUSSION

High-resolution, high-contrast MEMRI was implemented for lamina-specific anatomical imaging of the rat retina in vivo. Improved spatial resolution was made possible by using a small radiofrequency (RF) coil and improved contrast by Mn administration.

Seven bands of alternating bright and dark signal intensities were observed in normal rat retinas. Gd-DTPA contrast-enhanced MRI studies confirmed the vascular boundaries of the retina and facilitated layer assignments. To further corroborate layer assignment, the retina of RCS rats whose photoreceptors are known to completely degenerate by P90 were studied. Indeed, MEMRI revealed the P90 RCS retinas were missing the outer plexiform layer, outer nuclear layer, and photoreceptor-segment layer. Finally, MRI laminar thicknesses were quantified and their layer assignments cross-validated against standard histology. To our knowledge, this is the first MRI study that

Table 1

Laminar Thickness (μm , Mean \pm SD) of Normal Sprague-Dawley ($n = 5$) and P90 RCS Retinas ($n = 5$) as Determined by MRI and Histology

Band	Pre-Gd	Post-Gd	Histology	Assignment
#1	65 ± 31	43 ± 16	31 ± 6	ganglion cell layer + nerve fiber layer
#2	50 ± 3	47 ± 9	61 ± 4	inner plexiform layer
#3	38 ± 6	38 ± 5	39 ± 6	inner nuclear layer
#4	30 ± 7	33 ± 3	14 ± 3	outer plexiform layer
#5	24 ± 1	28 ± 10	53 ± 8	outer nuclear layer
#6	28 ± 3	30 ± 5	53 ± 8	inner + outer segment
#7	44 ± 10^a	63 ± 13^a	18 ± 3	choroidal vascular layer
Total	275 ± 30^b	279 ± 30^b	252 ± 5	

^a $P < 0.05$. The choroidal vascular layer post-Gd-DTPA was slightly thicker than pre-Gd-DTPA, likely due to the increased PVE associated with the marked increase in signal intensity. Both MRI determinations of choroidal vascular layer were statistically different from histological thickness.

^bDetermined from the width of the entire retina including the choroid (not from summing up all the band thicknesses).

Table 2
Laminar Thickness (μm , Mean \pm SD, $n = 5$) of the P90 RCS Retina Determined by MRI and Histology

Band	MRI	Histology	Assignment
#1	37 \pm 3	25 \pm 10	ganglion cell layer + nerve fiber layer
#2	26 \pm 5	61 \pm 4	inner plexiform layer
#3	21 \pm 14	43 \pm 9	inner nuclear layer
#4			
#5	25 \pm 8	29 \pm 11	debris layer
#6			
#7	32 \pm 8	31 \pm 2	choroidal vascular layer
Total	212 \pm 22 ^a	173 \pm 25 ^a	

^aDetermined from the width of the entire retina including the choroid (not from summing up all the band thicknesses).

demonstrates histologically defined multilayer structures of the retina in vivo at high spatial resolution and contrast.

Comparison With Lamina-Specific MRI Without Mn Injection

Lamina-specific structures and thicknesses of the rat (8) and cat (13) retina using MRI without Mn injection and at lower spatial resolution have been reported previously. In these studies, only three alternating bright and dark bands were observed. The total thickness of rat retina, including the choroidal vascular layer, was 267 \pm 31 μm by MRI and 205 \pm 11 by histology (8), in agreement with values reported herein. The total thickness of the feline retina, however, was significantly thicker (358 \pm 13 μm by MRI and 319 \pm 77 μm by histology (13)), due to the presence of an additional tapetal layer (87 \pm 35 μm by histology (13) behind the RPE, which facilitates low-light vision (14). The Mn-enhanced MRI presented here demonstrated improved resolution and contrast sufficient to visualize additional and histologically defined laminar structures that were not detectable by previous MRI.

Technical Considerations

The optimal (lowest) dose of MnCl_2 required to obtain consistent contrast enhancement of different layers in the retina was determined to be 5 μL of 30 mM MnCl_2 solution when imaged 24 hours after injection. Higher concentrations of MnCl_2 (ie, 120 mM) resulted in undesirable T_2^* signal decay, particularly in the retinal layers closest to the vitreous (such as the ganglion cell layer). Lower dose (i.e., 20 mM), on the other hand, yielded insufficient or inconsistent contrast to reliably differentiate retinal layers. Our optimal dose was lower than those reported previously that employed intravitreal injection of MnCl_2 (2 μL and 800 mM (15,16) and 3 μL and 50 mM (17–20)). Although the intraocular pressure was not monitored, MRI and visual inspection did not reveal significant shape distortion following intravitreal Mn injection. In some animals, histology was also performed on the noninjected right eyes to evaluate the potential toxicity of intravitreal Mn injection. Gross histology and

behavioral assessment also did not show obvious toxicity or changes in retinal thickness within 24 hours of intravitreal Mn injection (data not shown). Acute and chronic Mn toxicity in the retinas remains to be vigorously investigated.

PVE and Limitations of Thickness Determination

While the spatial resolution herein compares favorably with the published literature, potential PVE when imaging retinal layers exists because the retina is thin and curved. Given the spatial resolution, imaging slice thickness employed, and the total retinal thickness in rats, PVE (8,11) was calculated to be negligible (<10%) when MEMRI was used to determine total retinal thickness (data not shown). Indeed, MRI and histologic determinations of total retinal thickness were highly correlated. However, because each layer consists of only 1–3 pixels, some PVE on individual layer thickness determination is likely present in both slice-thickness and in-plane dimensions. Consequently, PVE may lead to overestimation of laminar thicknesses. Nonetheless, seven bands in the MRI images and intensity profiles were clearly resolved. MEMRI clearly and consistently documented the missing outer plexiform layer, outer nuclear photoreceptor layer, and photoreceptor-segment layer in the P90 RCS retinas, as confirmed by standard histology. The thickness determination based on intensity profiles was used instead of counting pixels within each band. This approach was sufficiently robust for laminar thickness comparison between normal and diseased retinas. To further minimize the PVE, the sum of individual layer thicknesses was constrained by total retinal thickness, which was validated independently. Thus, the overall conclusions with regard to MEMRI layer assignment are likely valid and are further justified below.

Justification of Layer Assignments

Following our initial observations of laminar structures, three different additional studies were performed to corroborate layer assignments, namely, studies using Gd-DTPA, RCS rat model of retinal degeneration, and standard histology. The Gd-DTPA results established the boundaries of the retina, set the upper limit of the retinal thickness, and thus assisted in making layer assignment. Consistent with the anatomy of embedded retinal vessels within these layers, bands #1–3 in MEMRI were assigned as the ganglion cell layer, inner plexiform layer, and inner nuclear layer, respectively, because these bands were enhanced by Gd-DTPA. Moreover, band #1 (ganglion cell layer) was more diffusely enhanced in MEMRI and its intensity was slightly lower than the other (inner and outer) nuclear layers (bands #3 and 5) and the choroid (band #7). This may be due to the relatively lower cell density of the ganglion cell layer compared to the other nuclear layers, consistent with histology. The RPE, a single-cell 5- μm -thick layer, sandwiched

between the choroid and the outer photoreceptor segments, is unlikely visible by MRI.

Mn enhanced band #7 heavily, to a similar or greater extent than the nuclear layers. One possible explanation is that endothelial cells that line the choroidal vessels strongly accumulate Mn, similar to the observation in the cerebral vascular endothelium (21,22). Band #7 was further and strongly enhanced by Gd-DTPA, confirming its vascularity. Band #7 was assigned as the choroidal vascular layer.

The RCS rats provided an excellent model to corroborate layer assignments. In contrast to the seven bands observed in the normal retinas, MEMRI of the P90 RCS retinas revealed only four bands, plus a debris band. Bands #4, #5, and #6 appeared to be missing, consistent with the known degeneration of the outer nuclear layer and the photoreceptor-segment layer in the P90 RCS retinas (9). The outer plexiform layer, which consists of the synaptic links from the photoreceptors, possibly degraded in response to the photoreceptors degeneration. Histology of the P90 RCS retinas confirmed the absence of the outer plexiform layer. Histologically, the outer plexiform layer, outer nuclear layer, and photoreceptor-segment layer appeared to coalesce into the debris layer. Bands #4–6 in the normal retina were thus assigned as the outer plexiform layer, outer nuclear layer, and photoreceptor-segment layer, respectively. In the P90 RCS retina, bands #4–6 constituted the debris layer.

In the P90 RCS retina, band #3 was hyperintense compared to band #2 and the debris band, suggesting that band #3 is a nuclear layer. Moreover, histology of band #3 in the P90 RCS retina appeared relatively normal, consistent with published data that the thickness of the inner nuclear layer remains largely intact (23), although subtle changes secondary to photoreceptor loss has also been identified (9). Such secondary effects could result in a lower Mn accumulation in band #3 of the P90 RCS retina relative to normal retina, as observed. In the normal retina, band #3 was further enhanced by Gd-DTPA, suggesting it is not part of the avascular regions of the retina. Band #3 was thus assigned as the inner nuclear layer.

In short, studies of the RCS retina made possible the layer assignments of bands #4, 5, and 6 and helped to assign band #3. Band #2, located between the ganglion cell layer and the inner nuclear layer, was weakly enhanced by Mn, consistent with it being a plexiform layer. Band #2 was also weakly enhanced by Gd-DTPA, consistent with the relatively lower vascular density of the embedded retinal vessels in the plexiform layer compared to the ganglion cell layer and the choroidal vascular layer. Band #2 was thus assigned as the inner plexiform layer.

Laminar Thickness

Histological correlation of laminar thicknesses further corroborated layer assignments. MEMRI-derived thickness of the entire neural retina ($\approx 235 \mu\text{m}$), excluding the choroidal vascular layer, is in good agreement with the total thickness of the rat neural retina reported using histology (24,25), ultrasound

(26), and optical coherence tomography (27,28). Importantly, thicknesses of individual layers determined by our histology are also in general agreement with those reported by histology (24) and ultrasound (26). MRI-derived band thicknesses were not statistically different from the corresponding histology-derived laminar thickness, except for band #7, the choroid vasculature. The choroidal vascular layer was measured to be $44 \pm 10 \mu\text{m}$ by MRI and $37 \pm 4 \mu\text{m}$ by histology. Reports of the choroidal vascular layer thickness are sparse. We only found one report of choroidal thickness by histology ($25\text{--}45 \mu\text{m}$) (29). This is perhaps not surprising because histological extraction of the choroid typically detaches between the photoreceptor and RPE, excluding the choroid from the mount. Optically based imaging techniques have difficulty in imaging the choroid because visible light does not readily penetrate the RPE. Similarly, ultrasound contrasts of the choroid appear ambiguous for laminar thickness determination. Possible explanations for the discrepancy between ex vivo and in vivo choroidal thickness are: 1) histology is susceptible to fixation shrinkage, 2) vessels in the extracted choroid collapse in the absence of blood flow, and 3) PVE of MRI could potentially overestimate choroidal thickness. Nonetheless, this is the first report of a choroidal vascular layer thickness measurement in vivo, underscoring the importance of in vivo measurements.

Future Perspective

While MEMRI will have limited human application, conventional MRI has been applied to study the human retina. Zhang et al (30) demonstrated blood oxygenation level-dependent (BOLD) functional MRI (fMRI) signal changes associated with oxygen and carbogen challenges in the unanesthetized human retina on a clinical 3 T scanner. These findings indicate that clinical scanners have sufficient signal-to-noise ratio (SNR), gradient strength, and stability to perform retinal BOLD fMRI in unanesthetized humans. Eye movement can be effectively managed with eye fixation, synchronized blinks, and postprocessing image coregistration. Maleki et al (31) also recently reported blood flow MRI of the human retina, albeit at lower spatial resolution. Peng et al (32) demonstrated that quantitative basal blood flow and its responses to hypercapnic challenge in unanesthetized human retina can be imaged using noninvasive MRI. While none of these studies thus far yielded laminar resolution, we predict that it will be possible. With rapid advances in MRI technologies to improve spatio-temporal resolution, we anticipate that MRI applications in the retina will broaden.

In summary, high-resolution MEMRI resolves lamina-specific structures in the rat retina in vivo without relying on optical transparency. This technique demonstrated the sensitivity and specificity to resolve laminar structures that correspond to layers outlined by histology. Further improvements in resolution, SNR, and contrast are expected. Extensions of established MRI technologies in the brain, including lamina-

specific measurements of stimulus-evoked calcium-dependent changes using MEMRI, lamina-specific MRI of blood flow, oxygenation and function of the retina, could open up new avenues for retinal research.

NOTE ADDED IN PROOF

Zhang et al recently demonstrated the feasibility of achieving high-resolution, layer-specific anatomical MRI in the awake human retina (33).

REFERENCES

- Wassle H, Boycott BB. Functional architecture of the mammalian retina. *Physiol Rev* 1991;1:447–480.
- Yu D-Y, Cringle SJ. Oxygen distribution and consumption within the retina in vascularised and avascular retinas and in the animal models of retinal disease. *Prog Retinal Eye Res* 2001;20:175–208.
- Cotzias G, Horiuchi M, Fuenzalida S, Mena I. Clearance of tissue manganese concentrations with persistence of the neurological picture. *Neurology* 1968;18:376–382.
- Takeda A, Kodama Y, Ishiwatari S, Okada S. Manganese transport in the neural circuit of rat CNS. *Brain Res Bull* 1998;45:149–152.
- Lee JH, Silva AC, Merkle H, Koretsky AP. Manganese-enhanced magnetic resonance imaging of mouse brain after systemic administration of MnCl₂: dose-dependent and temporal evolution of T1 contrast. *Magn Reson Med* 2005;53:640–648.
- Aoki I, Wu YJ, Silva AC, Lynch RM, Koretsky AP. In vivo detection of neuroarchitecture in the rodent brain using manganese-enhanced MRI. *Neuroimage* 2004;22:1046–1059.
- Berkowitz BA, Roberts R, Goebel DJ, Luan H. Noninvasive and simultaneous imaging of layer-specific retinal functional adaptation by manganese-enhanced MRI. *Invest Ophthalmol Vis Sci* 2006;47:2668–2674.
- Cheng H, Nair G, Walker TA, et al. Structural and functional MRI reveals multiple retinal layers. *Proc Natl Acad Sci U S A* 2006;103:17525–17530.
- Wang S, Villegas-Perez MP, Holmes T, et al. Evolving neurovascular relationships in the RCS rat with age. *Curr Eye Res* 2003;27:183–196.
- Strupp JP. Stimulate: a GUI based fMRI analysis software package. *Neuroimage* 1996;3:S607.
- Duong TQ, Muir ER. Magnetic resonance imaging of the retina. *Japanese J of Ophthalmology* 2009;53:352–367.
- Duong TQ, Pardue MT, Thule PM, et al. Layer-specific anatomical, physiological and functional MRI of the retina. *NMR Biomed* 2008;21:978–996.
- Shen Q, Cheng H, Pardue MT, et al. Magnetic resonance imaging of tissue and vascular layers in the cat retina. *J Magn Reson Imaging* 2006;23:465–472.
- Ollivier FJ, Samuelson DA, Brooks DE, Lewis PA, Kallberg ME, Komaromy AM. Comparative morphology of the tapetum lucidum (among selected species). *Vet Ophthalmol* 2004;7:11–22.
- Lin GP, Tseng WYI, Cheng HC, Cheng JH. Validation of diffusion tensor magnetic resonance axonal fiber imaging with registered manganese-enhanced optic tracts. *Neuroimage* 2001;14:1035–1047.
- Pautler R, Silva A, Koretsky A. In vivo neuronal tract tracing using manganese-enhanced magnetic resonance imaging. *Magn Reson Med* 1998;40:740–748.
- Chan KC, Fu QL, Hui ES, So KF, Wu EX. Evaluation of the retina and optic nerve in a rat model of chronic glaucoma using in vivo manganese-enhanced magnetic resonance imaging. *Neuroimage* 2008;40:1166–1174.
- Chan KC, Li J, Kau P, et al. In vivo retinotopic mapping of superior colliculus using manganese-enhanced magnetic resonance imaging. *Neuroimage* 2010;54:389–395.
- Thuen M, Berry M, Pedersen TB, et al. Manganese-enhanced MRI of the rat visual pathway: acute neural toxicity, contrast enhancement, axon resolution, axonal transport, and clearance of Mn(2+). *J Magn Reson Imaging* 2008;28:855–865.
- Thuen M, Singstad TE, Pedersen TB, et al. Manganese-enhanced MRI of the optic visual pathway and optic nerve injury in adult rats. *J Magn Reson Imaging* 2005;22:492–500.
- Lin Y-J, Koretsky AP. Manganese ion enhances T1-weighted MRI during brain activation: an approach to direct imaging of brain function. *Magn Reson Med* 1997;38:378–398.
- Duong TQ, Silva AC, Lee S-P, Kim S-G. Functional MRI of calcium-dependent synaptic activity: cross correlation with CBF and BOLD measurements. *Magn Reson Med* 2000;43:383–392.
- Yu D-Y, Cringle SJ, Su E-N, Yu PK. Intraretinal oxygen levels before and after photoreceptor loss in the RCS rat. *Invest Ophthalmol Vis Sci* 2000;41:3999–4006.
- Toprak AB, Ozbilgin K, Toprak V, Tuglu I, Guler C. A histological analysis of the protective effect of ischemic preconditioning in the rat retina. *Curr Eye Res* 2002;24:234–239.
- Joly S, Pernet V, Dorfman AL, Chemtob S, Lachapelle P. Light-induced retinopathy: comparing adult and juvenile rats. *Invest Ophthalmol Vis Sci* 2006;47:3202–3212.
- Jolly C, Jeanny JC, Behar-Cohen F, Laugier P, Saied A. High-resolution ultrasonography of subretinal structure and assessment of retina degeneration in rat. *Exp Eye Res* 2005;81:592–601.
- Thomas BB, Arai S, Ikai Y, et al. Retinal transplants evaluated by optical coherence tomography in photoreceptor degenerate rats. *J Neurosci Methods* 2006;151:186–193.
- Sho K, Takahashi K, Fukuchi T, Matsumura M. Quantitative evaluation of ischemia-reperfusion injury by optical coherence tomography in the rat retina. *Jpn J Ophthalmol* 2005;49:109–113.
- Steinle JJ, Krizsan-Aghas D, Smith PG. Regional regulation of choroidal blood flow by autonomic innervation in the rat. *Am J Physiol Regul Integr Comp Physiol* 2000;279:202–209.
- Zhang Y, Peng Q, Kiel JW, Rosende CA, Duong TQ. Magnetic resonance imaging of vascular oxygenation changes during hyperoxia and carbogen challenges in the human retina. *Invest Ophthalmol Vis Sci* 2011;52:286–291.
- Maleki N, Dai W, Alsop DC. Blood flow quantification of the human retina with MRI. *NMR Biomed* 2011;24:104–111.
- Peng Q, Zhang Y, Nateras OS, van Osch MJ, Duong TQ. MRI of blood flow of the human retina. *Magn Reson Med* 2011;65:1768–1775.
- Zhang Y, Oscar San Emeterio Nateras O, Peng Q, et al. Lamina-specific anatomical magnetic resonance imaging of the human retina. *Invest Ophthalmol Vis Sci* 2011;52:7232–7237.